Ultrasonics 125 (2022) 106795

Contents lists available at ScienceDirect

Ultrasonics

journal homepage: www.elsevier.com/locate/ultras

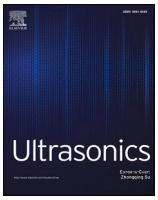

Interaction of three-dimensional acoustic beam with fluid-loaded solid plate: Axial near- to far-field transmission at normal beam incidence

M.M. Sæther [*], S.H. Midtbø [1], P. Lunde

University of Bergen, Department of Physics and Technology, Bergen, Norway

ARTICLE INFO

Keywords:
Leaky Lamb waves
Angular spectrum modeling
Axial nearfield effects of water-immersed plate
Ultrasonic beam transmission through plate at normal incidence

ABSTRACT

Axial radiation from leaky Lamb waves propagating in a 6.05 mm water-immersed steel plate being excited by a sound beam normally incident to the plate, is investigated as a function of axial distance, z, and frequency, f, over the 350–1000 kHz frequency band of the S_2, A_2, and A_3 Lamb modes in the plate. For certain leaky Lamb modes, prior literature has revealed complex characteristics in the transmitted pressure field close to the plate, caused by diffraction due to the finite angular spectrum of the incident beam. The present work extends earlier work by bringing insight into the changes of these field characteristics in the near- and far-field of the transmitted beam, over the frequency band of leaky Lamb modes, for normal beam incidence to the plate. A baffled piston source in a full-wave angular spectrum propagation model is used to analyze the phenomena involved. Maxima and minima that can not be described with plane wave theory are observed in the frequency spectrum of the axial pressure transfer function through the plate. At very long ranges the normalized transmitted sound beam tends to attain characteristics of the plate's plane-wave transmission coefficient, for two of the leaky Lamb modes. Near-field interference phenomena not described in prior literature are identified. For the leaky Lamb mode associated with a backward-wave branch close to the fundamental thickness-extensional resonance in the plate, TE1, the axial near-field is shown to extend to very far ranges. Supplementary measurements add confidence to the simulation results and findings. Besides of their fundamental significance in the study and understanding of sound beams transmitted through a fluid-immersed solid plate, the results are of importance e.g. in immersion applications where material characterization is made using fluid-coupled ultrasonic transducers in a through-thickness resonant transmission setup, such as plate thickness or material properties measurements.

1. Introduction

Sound beams reflected from and transmitted through a homogeneous, isotropic, elastic, and fluid-embedded plate have been extensively studied [1–33]. The interaction of the incident sound with the plate excites propagating leaky Lamb waves in the plate that radiate sound into the embedding fluid.

For beams normally incident to the plate, anomalous phenomena have been reported for the transmitted sound pressure field in the frequency band of the fundamental plane-wave thickness-extensional resonance of the plate, TE1. This includes (i) down-shifted frequency of the maximum in the pressure frequency spectrum associated with TE1, as compared to the TE1 resonance frequency [15,18,27,28]; (ii) increased transmitted axial sound pressure level (SPL) at this maximum, as compared to the incident axial free-field SPL at the upper surface of the plate [18–20,27,28], and (iii) narrowing of the transmitted beam, as compared to the incident beam [18,23,24,27,28]. For the first overtone plane-wave thickness-extensional resonance of the plate, TE2, widening of the transmitted beam has been reported [23,24,27,28]. Simulations of these phenomena using realistic piezoelectric transducer beam fields have been supported by measurements at a close distance from the plate [22,23,27,28].

The phenomena observed in the frequency band close to TE1 have been ascribed to interaction of the finite angular spectrum of the normally incident beam with the backward-wave branches [34] of the S_2 and S_{-2} symmetric Lamb modes in the plate [28]. In backward waves the phase and group velocities are of different sign [34]. For the negative and positive in-plane ("horizontal") wavenumbers of the backward-wave branches of S_2 and S_{-2}, respectively, the group velocity is positive and negative [35–38], respectively. For the portion of the incident

* Corresponding author.
E-mail address: mathias.sather@uib.no (M.M. Sæther).
[1] Currently with Norwegian University of Science and Technology, Trondheim, Norway.

https://doi.org/10.1016/j.ultras.2022.106795
Received 10 November 2021; Received in revised form 10 June 2022; Accepted 14 June 2022
Available online 17 June 2022

beam's angular spectrum that interacts with the backward-wave branches, the backward waves effectively confine the beam in the plate direction by carrying energy back into the beam center [4]. For spectral portions that interact with forward wave branches, energy is carried away from the beam center. These mechanisms appear to be the explanation for the observed concentration of energy in the (narrowed) transmitted beam, the accompanying increase of SPL through the plate, and the lowered resonance frequency of the plate. The negative group velocity of the backward-wave branch of S_{-2} has been interpreted by different authors as a coupling effect between shear and compressional waves in the plate near cutoff [4], or due to mode repulsion between even and odd modes of the same type [38,39]. Detailed knowledge of the physics underlying the observed phenomena is of significance in the study and understanding of sound beams transmitted through a fluid-immersed solid plate, and in practical applications based on the use of spectral resonances in the plate.

Applications in this area include characterization of materials using fluid-coupled ultrasonic transducers in a resonant reflection or transmission immersion setup. Examples are measurement of plate and pipe wall thickness [3,4,11,15,25,40–42], e.g. for corrosion inspection, compressional- or shear-wave bulk velocities [7,12,16,17,41–44], and inspection and imaging of discontinuities and inhomogeneities [45]. The through-thickness resonance method is commonly used [25,33,41,42,45]. The spectral maxima or minima in the pressure field measured at some distance from the plate, may be interpreted in terms of one or several plane-wave thickness-extensional (TE) or thickness-shear (TS) resonances in the plate. In use of TE1 for such measurements, the downshifted thickness resonance frequency will require a "finite-aperture correction" for the downshift when accuracy in measurement is of importance.

Another example of relevance is the detection or characterization of one or several objects behind a fluid-embedded plate or pipe wall, using e.g. a transmission-reflection immersion setup. Knowledge of the sound field transmitted through the plate in relevant positions of the object(s), including possible anomalies in this field, is then of importance for the outcome of the measurement.

In such applications, using finite-aperture transducers and operation in the frequency band of TE1 or other TE or TS plate resonances, several questions arise: (1) To what extent does already known bounded beam phenomena depend on the distance from the plate to the receiving transducer, for the relevant spectral maxima and minima in the transmitted field?; (2) Would there be additional bounded beam phenomena not discovered in prior studies, e.g. at specific frequencies and distances from the plate?; (3) To which extent may bounded-beam phenomena influence when the characterization measurement is interpreted using common plane-wave theory for TE and TS resonances?; (4) What are the characteristics and spatial extent of the transmitted near-field, for the various leaky Lamb modes involved, as a function of frequency and increasing distance from the plate?

In relation to such questions for transmitted beams, there appears to be no near- to far-field studies reported on possible changes of spectral maxima and minima observed, as compared with the corresponding TE or TS resonances. Earlier work has focused on close distance from the plate [18–24,26–29,31,32]. From studies of reflected beams, however, it has been shown that as the transducer-plate distance increases, an observed downshift of the resonant notch being associated with TE1 is monotonically reduced [3,4]. In the TE1 frequency band the "effective" reflection coefficient asymptotically approaches the plane-wave reflection coefficient of the plate [4]. For the notch associated with TE2, a slight monotonic downshift with increasing distance from the plate has been observed [3]. Similar effects may thus possibly be expected for beam transmission. In contrast to the reflection studies reported in [3,4], it would be of interest to keep the source-plate distance constant (in the far-field of the source), while the plate-receiver distance is varied.

The objective of the present work is to investigate such questions in a simulation study. A 6.05 mm thick water-immersed steel plate of infinite extent is excited by a sound beam at normal incidence to the plate. Near-field phenomena in the plate's axial pressure transfer function, $|H_{pp}|$, including radiation from leaky Lamb waves propagating in the plate, are investigated along the beam axis as a function of frequency and increasing distance from the plate. Frequencies in the range 350–1000 kHz are considered, covering the frequency band of certain lower leaky Lamb modes. Distances up to 500 m from the plate have been found necessary to gain sufficient insight into the detailed near- to far-field transition characteristics of the transmitted beam. A baffled piston source combined with a full-wave angular spectrum propagation model (ASM) is used. Here and in the following, "piston" refers to a planar circular piston source mounted in a rigid baffle of infinite extent, vibrating with uniform particle velocity. Changes in shape, bandwidth, level, dynamics, and frequencies of spectral maxima and minima in $|H_{pp}|$ are compared with (i) the plate's plane-wave pressure transmission coefficient, $|T|$, and (ii) the cutoff frequencies of the associated Lamb modes of the traction-free plate, vibrating in vacuum. For added confidence, the simulation results are compared with measurements of the transmitted beam at three axial distances from the plate using a 575 kHz transducer operating over the same frequency range.

The theoretical basis of the ASM piston model is presented in Section 2. The experimental and simulation setups are described in Sections 3 and 4, respectively. Results are presented and discussed in section 5, with conclusions given in Section 6.

2. Theory

An angular spectrum model (ASM) [30] for investigation of beam transmission through a fluid-immersed solid plate at normal beam incidence is presented, in which the incident beam is described as the field radiated by a circular and baffled piston source. The following model capabilities are needed, extending prior approaches used for such problems [10,19,20,22,24,25,28]: (i) uniform (constant) particle velocity at the piston source; (ii) full angular (or wavenumber) spectrum description of the piston's near- and far-field regions using cylindrical coordinates, accounting for propagating and evanescent wave contributions; and (iii) pressure "reception" in a single point, where the source-plate and plate-receiver distances can be varied independently.

The setup used for mathematical-numerical modeling [30] is shown in Fig. 1. A steel plate of thickness d is immersed in a fluid. The plate is assumed to be elastic, isotropic, homogeneous, and of infinite lateral extent. A circular and baffled piston source, representing an ultrasonic transducer, generates an acoustic beam field that is transmitted through

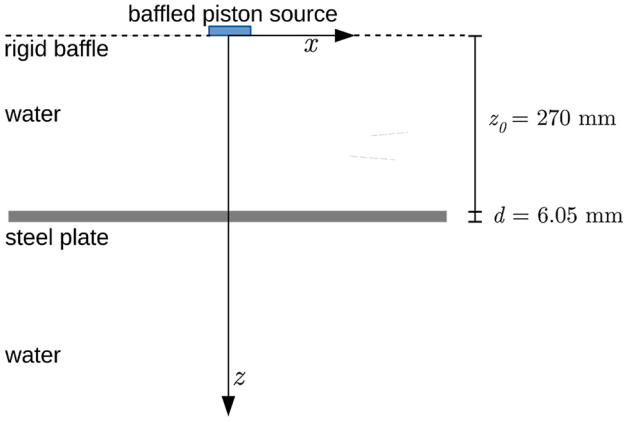

Fig. 1. Schematics of the setup used for mathematical-numerical modeling. A baffled circular piston source is vibrating uniformly in a fluid (water). A steel plate of thickness d and infinite lateral extent is located at distance z_0 from the piston front surface. The model is angular symmetric about the z axis.

the fluid-immersed plate at normal beam incidence to the plate. The piston surface is oriented parallel to the plate, at a distance z_0 from the plate. A Cartesian coordinate system is indicated, with origin at the center of the piston surface, the x and y axes in the source plane $z = 0$, the z axis normal to the piston surface, and the y axis pointing out of the paper. The fluid is assumed to be homogeneous, with constant sound velocity, c_f, and density, ρ_f. The plate material and the fluid medium are taken to be lossless.

The ASM model is expressed in cylindrical coordinates (r,θ,z), where $r = \sqrt{x^2 + y^2}$ is the radial range and θ is the polar angle (in the x-y plane). For the axisymmetric model setup (angular symmetry about the z axis) θ is superfluous and omitted. A time convention $e^{i\omega t}$ is used and suppressed, where $\omega = 2\pi f$ is the angular frequency and f is the frequency. The argument of the field quantities is thus the vector (r,z,f).

The plate's acoustic response at the acoustic axis ($r = 0$) is studied using the axial pressure transfer function

$$H_{pp}(0,z,f) = \frac{p(0,z,f)}{p_i(0,z_0,f)}. \tag{1}$$

$p_i(0,z_0,f)$ is the axial free-field sound pressure frequency spectrum radiated by the piston at range z_0 (i.e., the axial free-field sound pressure frequency spectrum incident to the plate, in absence of the plate). $p(0,z,f)$ is the axial sound pressure frequency spectrum transmitted through the steel plate at distance z. Both $p_i(0,z_0,f)$ and $p(0,z,f)$ are calculated using the ASM model as described in the following.

The z component of the piston's particle velocity frequency spectrum at frequency f is given as.

$$v_z(r,z=0,f) = \begin{cases} v_0, & r \le a, \\ 0, & r > a, \end{cases} \tag{2}$$

where v_0 is a constant and a is the piston radius. By Hankel transforming v_z, the particle velocity wavenumber spectrum in the source plane is given as [46] (p. 48)

$$V_z(\eta,0,f) = 2\pi \int_0^\infty v_z(r,0,f) J_0(\eta r) r dr = \pi a^2 v_0 \frac{2J_1(a\eta)}{a\eta}. \tag{3}$$

J_0 and J_1 are the zeroth and first order Bessel functions of the first kind, respectively. η is the component of the acoustic wave vector in the plane of the plate (the r-direction), here referred to as the "horizontal wavenumber" (or simply the "wavenumber"). In the present work only real-valued η are considered, since no sources or inhomogeneities within the plate are present, eliminating the need for imaginary- and complex-valued η, associated, respectively, with evanescent and propagating waves that are rapidly decaying in the plate (r) direction [47]. The z-component of the linearized Euler's equation in the frequency domain is given as.

$$i\omega\rho_f v_z(r,z,f) = -\frac{\partial p(r,z,f)}{\partial z}. \tag{4}$$

A spatial Hankel transform with respect to r yields

$$i\omega\rho_f V_z(\eta,z,f) = -\frac{\partial P(\eta,z,f)}{\partial z} = i h_{f,z} P(\eta,z,f), \tag{5}$$

for a plane wave propagating in the positive z direction at a given η and a given angle θ (arbitrary). Here, $V_z(\eta,z,f)$ and $P(\eta,z,f)$ are the particle velocity and sound pressure wavenumber spectra, respectively. From Eqs. (3) and (5) one finds

$$P(\eta,0,f) = \frac{\omega a \rho_f}{\eta h_{f,z}} 2\pi v_0 J_1(a\eta), \tag{6}$$

where

$$h_{f,z} = \begin{cases} \sqrt{h_f^2 - \eta^2}, & \eta \le h_f, \\ -i\sqrt{\eta^2 - h_f^2}, & \eta > h_f, \end{cases} \tag{7}$$

is the z component of the acoustic wave vector in the fluid (the "vertical wavenumber"), and $h_f = \omega/c_f$ is the acoustic wavenumber in the fluid. For $\eta > h_f$, $h_{f,z}$ becomes imaginary, representing evanescent (exponentially decaying) waves in the z direction.

$P(\eta,0,f)$ given by Eq. (6) is then propagated to a distance z_0 in the fluid using the plane-wave propagation term $e^{-ih_{f,z}z_0}$ [46], giving.

$$P_i(\eta,z_0,f) = P(\eta,0,f) e^{-ih_{f,z}z_0}. \tag{8}$$

Here, P_i is the wavenumber spectrum of the incident free-field sound pressure spectrum p_i in the fluid, at the upper surface of the plate, in absence of the plate.

$P_i(\eta,z_0,f)$ given by Eq. (8) is then first propagated in the z direction through the plate using the plate's plane-wave transmission coefficient, T, and secondly through the fluid beneath the plate using the plane wave propagation term $e^{-ih_{f,z}(z-d-z_0)}$, giving, for $z > z_0 + d$,

$$P(\eta,z,f) = P_i(\eta,z_0,f) T(\eta,d,f) e^{-ih_{f,z}(z-d-z_0)} = P(\eta,0,f) T(\eta,d,f) e^{-ih_{f,z}(z-d)}. \tag{9}$$

The plane-wave pressure transmission coefficient of the plate is defined as [10]

$$T(\eta,d,f) = \frac{P(\eta,z_0+d,f)}{P_i(\eta,z_0,f)}, \tag{10}$$

where $P(\eta,z_0+d,f)$ is the sound pressure wavenumber spectrum in the fluid at the plate's lower surface. T can be expressed as [10].

$$T(\eta,d,f) = \frac{-iY(A+S)}{(S+iY)(A-iY)} \tag{11}$$

where.

$$\begin{aligned} Y &= \frac{\rho_f h_z}{\rho h_{f,z}} k^4, \\ S &= \left(2\eta^2 - k^2\right)^2 \cot\left(h_z \frac{d}{2}\right) + 4\eta^2 h_z k_z \cot\left(k_z \frac{d}{2}\right), \\ A &= \left(2\eta^2 - k^2\right)^2 \tan\left(h_z \frac{d}{2}\right) + 4\eta^2 h_z k_z \tan\left(k_z \frac{d}{2}\right). \end{aligned} \tag{12}$$

Here, ρ is the plate density. h_z and k_z are the z components of the longitudinal and shear wave vectors in the plate, given as.

$$h_z = \begin{cases} \sqrt{h^2 - \eta^2}, & \eta \le h, \\ -i\sqrt{\eta^2 - h^2}, & \eta > h, \end{cases} \tag{13}$$

and

$$k_z = \begin{cases} \sqrt{k^2 - \eta^2}, & \eta \le k, \\ -i\sqrt{\eta^2 - k^2}, & \eta > k, \end{cases} \tag{14}$$

respectively. $h = \omega/c_l$ and $k = \omega/c_t$ are the longitudinal and shear wavenumbers, and c_l and c_t the longitudinal and shear wave velocities in the plate, respectively.

The sound pressure frequency spectra p_i and p are obtained by taking the inverse Hankel transform of Eqs. (8) and (9), respectively, giving

$$p_i(r,z_0,f) = \frac{1}{2\pi} \int_0^\infty P_i(\eta,z_0,f) J_0(\eta r) \eta d\eta \tag{15}$$

and

$$p(r,z,f) = \frac{1}{2\pi}\int_0^\infty P(\eta,z,f)J_0(\eta r)\eta d\eta. \quad (16)$$

The axial values of p_i and p used in Eq. (1) are then obtained at $r = 0$.

3. Experimental setup

Measurement results reported in [30] are used to compare with simulations. Fig. 2 shows the water tank in top view (with height 60 cm, width 75 cm, length 160 cm) and side view (with the y-z plane at x = 0, and the x axis pointing out of the paper). The center of the transducer's front surface is located at x = y = z = 0, where x = y = 0 is approximately the mid point of the tank's cross-sectional plane.

A piezoelectric transducer with center frequency 575 kHz was used; -designed, built, and characterized for measurements and finite element studies [23]. A 130 μs voltage tone burst generated by the HP 33120A signal generator excites the transducer over a frequency range 350–1000 kHz at 1 kHz frequency steps. For an assumed constant effective piston radius of $a = 10.55$ mm (obtained from the transducer's −3dB beamwidth measured at 575 kHz) [23], the ranges of the piston's $h_f a$ number, −3dB angle, and Rayleigh distance, are 15.6–44.6, 5.9−2.1°, and 82–235 mm, respectively, over the frequency band considered.

The acoustic pressure generated by the transducer was transmitted through a $d = 6.05$ mm thick AISI 316L stainless steel plate with lateral dimensions 500 and 760 mm in the x and y directions, respectively. The plate was located in the transducer's far-field at a source-plate distance $z_0 = 270$mm, corresponding to 3.3–1.2 Rayleigh distances in the piston model, over the frequency band considered.

The axial (x = 0, y = 0) acoustic pressure, p, was measured at distances z = 376.05, 626, and 875 mm, i.e., 100.00, 349.95, and 598.95 mm beneath the lower surface of the plate, using a calibrated Precision Acoustic PVDF needle hydrophone (1 mm diameter, 100 mm length). In addition, the free-field axial acoustic pressure, p_i, was measured at distance $z_0 = 270$ mm. For each frequency, $|H_{pp}|$ of Eq. (1) was obtained from the corresponding voltage amplitudes at that frequency. Further details on the experimental setup are given in [23].

In Section 5, the measurement results are reported in terms of the transfer function given in Eq. (1). It is noted that measurements are used here only for qualitative comparison with the simulations; to add confidence to the results, and for discussion of phenomena observed. Close quantitative agreement with simulation results can not be expected, since the measurements are made using a transducer, whereas the simulations are made using an ideal piston source.

4. Simulation setup

In the simulation setup shown in Fig. 1, a piston source with radius $a = 10.55$ mm [23] and $v_0 = 1$ m/s [30] is located at distance $z_0 = 270$ mm from a water-embedded steel plate of infinite extent and thickness $d = 6.05$ mm. The sound velocity in water is $c_f = 1485$ m/s. The plate and water densities are set to $\rho = 8000$ kg/m^3 and $\rho_f = 1000$ kg/m^3, respectively [23]. The plate's longitudinal and shear wave velocities are $c_l = 5780$ m/s and $c_t = 3130$ m/s [23], corresponding to a Poisson's ratio of 0.2925. Frequencies in the range 350–1000 kHz are used.

For each z and f, the integrals in Eqs. (15) and (16) are solved numerically using the trapezoidal rule, where the upper integration limit is set to $\eta_{max} = h_f + 400$ rad/m. For $\eta > \eta_{max}$, the magnitude of the integrands in Eqs. (15) and (16) are more than 500 dB lower than the average integrand magnitude for η in the region 0 to η_{max}, and thus negligible. This upper limit is frequency dependent, giving η_{max} in the range 2480–5240 rad/m over the frequency range.

To ensure sufficient integration accuracy, a non-uniform wavenumber (η) sampling strategy is used. In the simulations of $p_i(0,z_0,f)$ using Eq. (15), an accuracy better than 10^{-4} dB in magnitude has been achieved over the frequency range. For the simulations of $p(0,z,f)$ using Eq. (16) an accuracy better than 10^{-6} dB in magnitude has been achieved over the same frequency range, up to z = 40 m. For z = 500 m the accuracy is better than 10^{-6} dB, at the 478 kHz frequency component shown here. (An exception is the simulation of $p(0,z,f)$ shown in Fig. 5, for which the accuracy is within 10^{-2} dB in magnitude. The results in Fig. 5 are however used only for visual overview purposes and not to report quantitative results.) Possible errors less than these numbers are too small to affect any maxima or minima in the frequency spectra being discussed in the current work.

The general frequency resolution in the simulations is 100 Hz. Close to sharp spectral maxima and minima in Figs. 4 and 8, a frequency resolution as low as 0.5 Hz has been used. The Δz resolution in Figs. 5-6 is 10 mm.

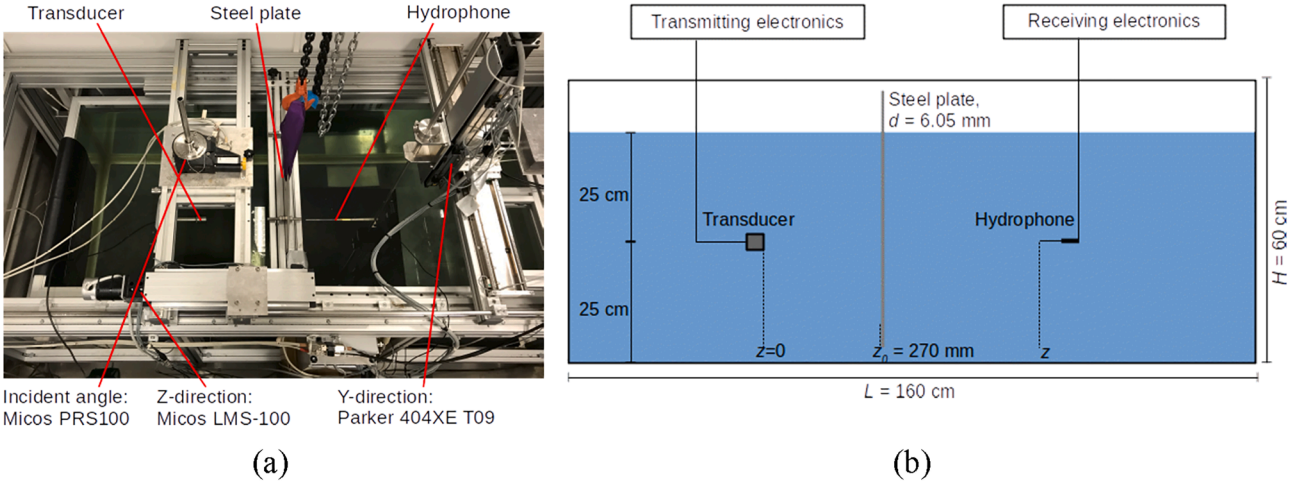

Fig. 2. Measurement setup in the water tank. (a) Photograph in top view, showing the transmitting transducer, steel plate, hydrophone and the positioning stages. (b) Drawing of the setup in side view (y-z plane, at x = 0). The water level is approximately 50 cm and the transducer and hydrophone are positioned approximately 25 cm above the bottom. Measurements are conducted at z = 376.05, 626, and 875 mm (10.000, 34.995, and 59.895 cm from the plate, respectively).

5. Results and discussion

5.1. Dispersion curves, Lamb mode cutoff frequencies, and frequencies of spectral maxima

In the following discussion of near-field and far-field effects in beam interaction with a fluid-embedded solid plate, the Lamb mode cutoff frequencies of the plate (i.e., the plane-wave cutoff frequencies of the corresponding traction-free plate vibrating in vacuum) will be useful reference frequencies.

Fig. 3 shows the magnitude of the plane-wave transmission coefficient for a water-embedded steel plate, $|T(\eta,d,f)|$, as a function of frequency f and angle of plane-wave incidence θ, calculated using Eqs. (11)-(14). Here, $\theta = \sin^{-1}(\eta/h_f)$, for $\eta \leq h_f$. The overlayed black dashed curves in Fig. 3 give the dispersion curves for the associated Lamb modes in the plate (i.e., vibrating in vacuum), calculated for real η. The symmetric and antisymmetric Lamb modes being present in the f-θ range shown are marked by S_0, S_1, S_2, S_{-2} and A_0, A_1, A_2, A_3, respectively.

Using the terminology of Aanes et al. [28], the plane-wave cutoff frequencies of the S_2, A_2, and A_3 Lamb modes of a solid plate with Poisson's ratio in the range 1/5–1/3, are labeled f_{l1}^S, f_{t2}^S, f_{t3}^A, and f_{l2}^A, respectively. S_2 is the 3rd symmetric Lamb mode, and A_2 and A_3 are the 3rd and 4th antisymmetric Lamb modes, respectively [48]. f_{l1}^S and f_{t2}^S are the lower and upper cutoff frequencies of the S_2 mode [48]. f_{t3}^A and f_{l2}^A are the cutoff frequencies of the A_2 and A_3 modes. Table 1 gives expressions and calculated figures for the four cutoff frequencies. These Lamb mode cutoff frequencies are indicated in Fig. 3.

Equivalently, expressed in terms of the TE and TS resonances of the plate, f_{l1}^S and f_{l2}^A are the resonance frequencies of the 1st and 2nd plane-wave thickness-extensional resonances in the plate, TE1 and TE2. f_{t2}^S and f_{t3}^A are the resonance frequencies of the plate's 2nd and 3rd plane-wave thickness-shear resonances, TS2 and TS3, cf. Table 1.

It should be noted that in the literature in this field, f_{l1}^S is often described as the cutoff frequency at the frequency axis of the 2nd symmetric Lamb mode, S_1 [49,50,51]. In the present work, in coherence with the complex dispersion curve description given by Mindlin [34,48], the S_2 Lamb mode is interpreted as having two cutoff frequencies at the frequency axis, here denoted the lower and upper cutoff frequencies of the S_2 mode, f_{l1}^S and f_{t2}^S, cf. Table 1. In this description S_1 has no cutoff frequency at the frequency axis.

It is noted that f_{l1}^S and f_{t2}^S are also the lower and upper cutoff frequencies of the S_{-2} mode [28,48], but for simplicity in discussion they will here be associated with the S_2 mode only.

For acoustic beam incidence, the frequencies of those maxima in the sound pressure frequency spectrum and the axial pressure transfer function $|H_{pp}|$ that are associated with the lower cutoff frequency of the S_2 Lamb mode and the A_3 Lamb mode (i.e., the TE1 and TE2 plate resonances), respectively, will in the sequel be labeled f_1 and f_2.

5.2. Change of $|H_{pp}|$ with z and f

Fig. 4 shows simulations and measurements of $|H_{pp}(0,z,f)|$ at z = 376.05 mm, 626 mm, and 875 mm, together with simulations at z = 40 m, plotted as a function of frequency. The vertical lines give the cutoff frequencies of the corresponding Lamb modes in the plate, cf. Table 1.

In the simulation results at z = 376.05 mm (Fig. 4(a)), the spectral maximum observed at $f_1 \approx 458$ kHz is associated with TE1, i.e., with S_2 at its lower cutoff frequency. The spectral minimum at about 517 kHz is associated with TS2, i.e., with S_2 at its upper cutoff frequency. The maximum and minimum doublet observed at approximately 775 kHz

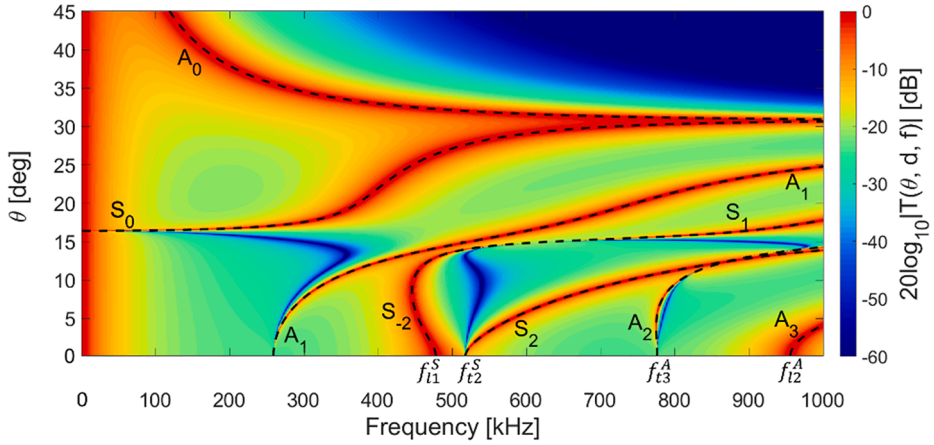

Fig. 3. Magnitude of the plane-wave pressure transmission coefficient $|T(\eta,d,f)|$, for a 6.05 mm steel plate in water, plotted together with dispersion curves (black dashed lines) for the associated Lamb modes of the plate vibrating in vacuum, as a function f and θ. Lamb modes and the four Lamb mode cutoff frequencies addressed in the sequel are indicated. For numerical calculations, values for c_l, c_t, and d are taken from Section 4. (Modified after [18].).

Table 1
Lamb mode cutoff frequencies for a steel plate of thickness d (a traction-free plate vibrating in vacuum), and their relationships to the S_2, A_2, and A_3 Lamb modes. The cutoff frequencies are the resonance frequencies of the plane-wave thickness-extensional (TE) and thickness-shear (TS) modes in the plate. For calculations, values for c_l, c_t, and d are taken from Section 4.

Lamb mode	3rd symmetric Lamb mode (S_2)		3rd antisymm. Lamb mode (A_2)	4th antisymm. Lamb mode (A_3)
	Lower cutoff	Upper cutoff		
Cutoff frequency	$f_{l1}^S = c_l/2d$ 477 686 Hz	$f_{t2}^S = 2c_t/2d$ 517 355 Hz	$f_{t3}^A = 3c_t/2d$ 776 033 Hz	$f_{l2}^A = 2c_l/2d$ 955 372 Hz
Plane-wave plate thickness resonance	1st thickness- extensional mode, TE1	2nd thickness-shear mode, TS2	3rd thickness-shear mode, TS3	2nd thickness-extensional mode, TE2

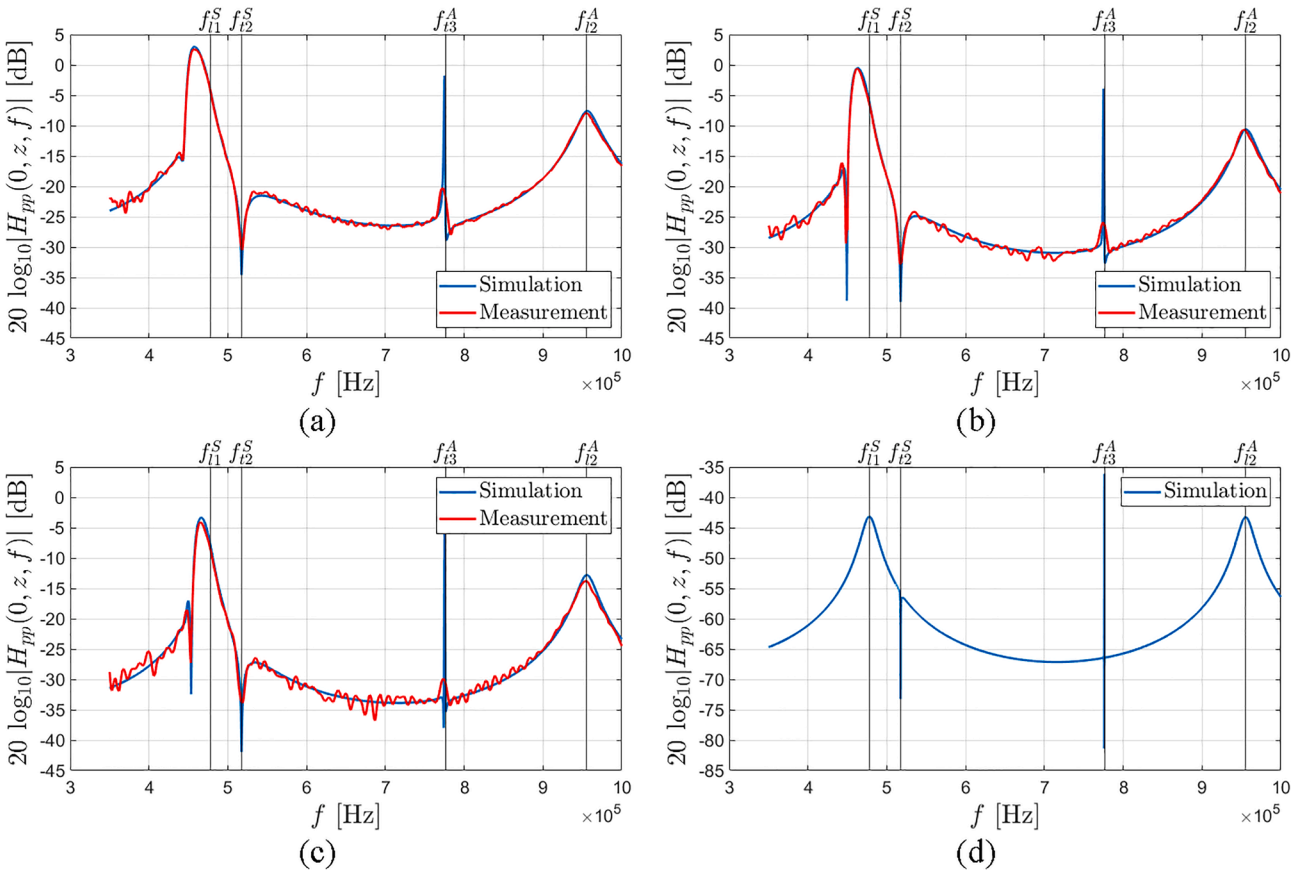

Fig. 4. Simulations and measurements [30] of $|H_{pp}(0,z,f)|$, for normal beam incidence to the plate, at (a) $z = 376.05$ mm, (b) $z = 626$ mm, and (c) $z = 875$ mm. (d) Corresponding simulation of $|H_{pp}(0,z,f)|$ at $z = 40$ m. The vertical lines in the plots show the Lamb mode cutoff frequencies $f_{l1}^S = 477.69, f_{t2}^S = 517.36, f_{t3}^A = 776.03$, and $f_{l2}^A = 955.37$ kHz, cf. Table 1.

are associated with TS3, i.e., with A_2. The maximum at $f_2 \approx 956$ kHz is associated with TE2, i.e., with A_3. In addition, a shallow spectral minimum ("notch") is observed below f_1, at approximately 443 kHz.

From $|T(\eta, d, f)|$ given in Fig. 3 it appears that the two shear resonances associated with TS2 and TS3 both appear as a maximum and minimum doublet, and that the two doublets are caused by wave interaction internally in the plate, due to the finite angular spectrum of the beam. In $|T|$ of Fig. 3 no event is identified that can be related to the notch at 443 kHz, which suggests that this notch is not due to wave interaction internally in the plate, but to destructive interference caused by the wave propagation in water.

At f_1 an increased SPL of about 3 dB for the transmitted field is observed, as compared to the incident field ($20\log_{10}|H_{pp}| \approx 3$ dB). These results at $z = 376.05$ mm are in agreement with earlier studies using this

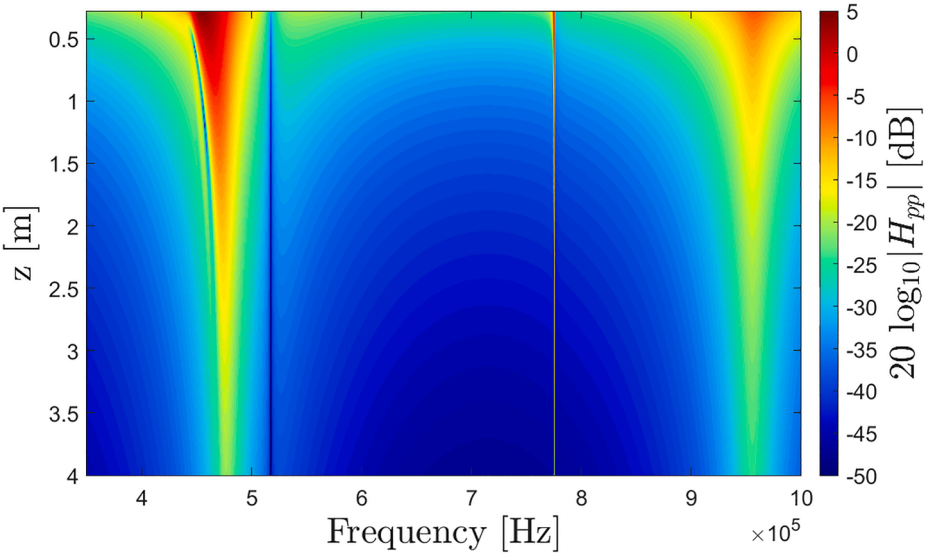

Fig. 5. Simulated $|H_{pp}(0,z,f)|$ over the frequency band 350 kHz – 1000 kHz and z in the range 276.05 mm (at the plate) to 4 m, using the ASM piston model.

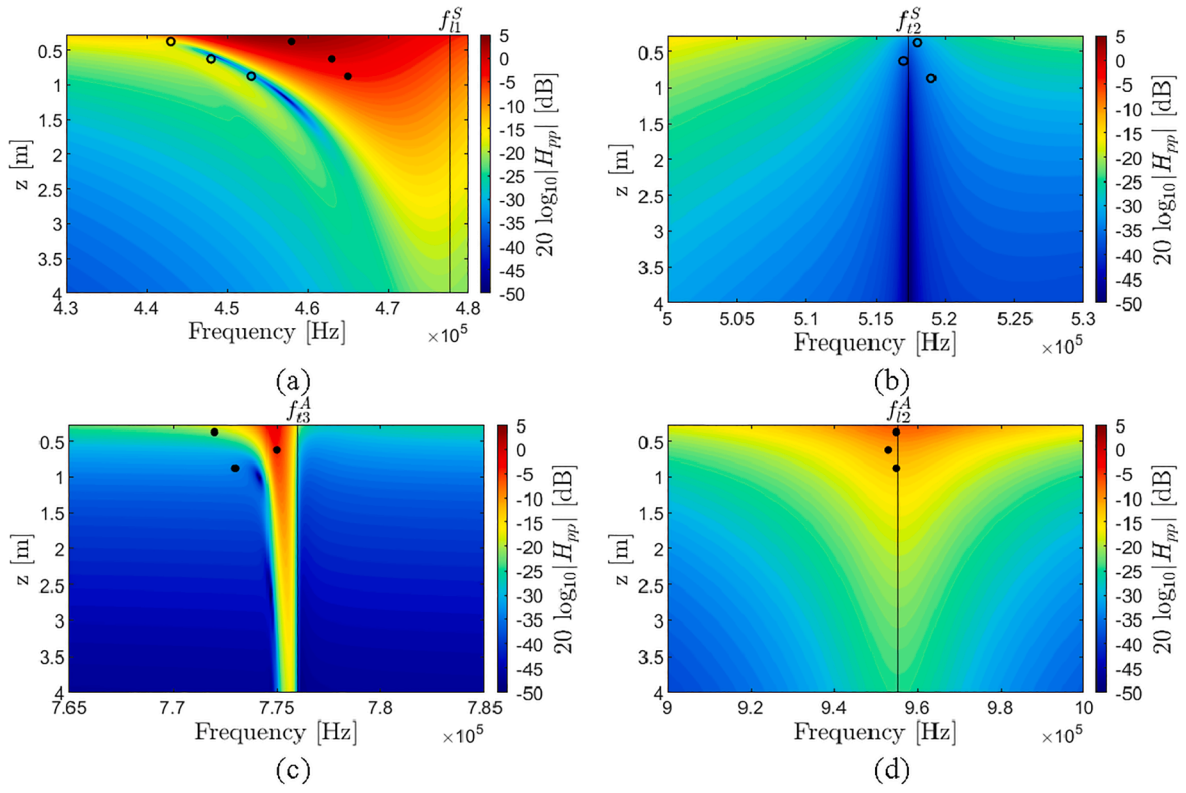

Fig. 6. Zoomed-in version of $|H_{pp}(0,z,f)|$ shown in Fig. 5, for frequency ranges (a) 430–480 kHz (in the vicinity of the S_2 Lamb mode's lower cutoff frequency, f_{l1}^S, i.e., TE1), (b) 500–530 kHz (in the vicinity of the S_2 Lamb mode's upper cutoff frequency, f_{t2}^S, i.e., TS2), (c) 765–785 kHz (in the vicinity of the A_2 Lamb mode's cutoff frequency, f_{t3}^A, i.e., TS3), and (d) 900–1000 kHz (in the vicinity of the A_3 Lamb mode's cutoff frequency, f_{l2}^A, i.e., TE2). The filled dots and open circle markers represent measured spectral maxima and minima, cf. Fig. 4. The vertical lines give the cutoff frequencies of the corresponding Lamb modes, cf. Table 1 and Figs. 3 and 4.

setup [18,19,23,27,28].

By increasing axial distance, z (Fig. 4(b)-(d)), simulated spectral maxima and minima in $|H_{pp}|$ are subject to frequency shift and change in magnitude and dynamics. At f_1, one finds $20\log_{10}|H_{pp}| < 0$ dB for all axial distances z shown in Fig. 4(b)-(d). The notch appearing below f_1 is very prominent at z = 626 mm, then more shallow at z = 875 mm, and totally absent at z = 40 m. Its frequency increases by increasing depth.

A fair quantitative agreement between measurements and simulations is observed in Fig. 4. Some deviation is found in description of the maximum-minimum doublet at the TS3 resonance, close to f_{t3}^A. In simulation the maximum and minimum are very narrow with high dynamics, whereas the measured response appears more damped. In the model intrinsic losses in the plate and water are not accounted for, which may be of significance for this deviation.

To investigate in further detail how spectral maxima and minima in $|H_{pp}|$ change with f and z, Fig. 5 shows the simulated $|H_{pp}(0,z,f)|$ for z in the range 276.05 mm (at the lower surface of the plate) to 4 m. In Fig. 6, the results of Fig. 5 are shown in more detail, for four "zoomed-in" frequency ranges close to TE1, TS2, TS3 and TE2, cf. parts (a), (b), (c), and (d), respectively. In addition, measured spectral maxima and minima from the experimental results given in Fig. 4 are shown with filled dot and open circle markers, respectively. The vertical lines give the cutoff frequencies of the associated Lamb modes.

In Fig. 6(a), the frequency band associated with TE1 and f_{l1}^S exhibits a complex near-field. At f_1 an increased SPL of about 5 dB is observed at the plate (at z = 276.05 mm) as compared to the incident field ($20\log_{10}|H_{pp}| \approx 5$ dB). f_1 is shifted upwards by increasing z, from about 455 kHz to about 478 kHz, accompanied by a reduction in SPL. The frequency downshifts of f_1 as compared with f_{l1}^S at z = 276.05, 376.05 mm and 4 m are about 4.8 %, 4.5 %, and 0.15 %, respectively. Causes of such downshift, and consequences for applications, are discussed in Sections 1 and 5.6.

A similar upwards frequency shift by increasing z is observed for the notch appearing below f_1, from about 440 to 468 kHz, in the z range of approximately 0.35–3.4 m. The minimum is particularly prominent for z in the ranges 0.6–0.7 m and 0.9–1.5 m. This can also be seen in the measurements and simulations shown in Fig. 4, for which the minimum is deeper for z = 626 mm as compared with z = 376.05 mm and 875 mm. The notch is discussed in Section 5.6.

In Fig. 6(b), in the frequency band associated with TS2 and f_{t2}^S, the frequency of the simulated spectral minimum is 517.4 kHz, which is within the 100 Hz frequency resolution as compared with the upper cutoff frequency of S_2, $f_{t2}^S = 517.36$ kHz. Within this frequency resolution, the frequency of this minimum is found to be constant over the z range 276.05 mm to 4 m. Potentials for plate characterization using finite-aperture transducers are significant, as discussed in Section 5.6.

In the frequency region of the TS3 plate resonance, $|H_{pp}(0,z,f)|$ exhibits a rather complex behavior, cf. Fig. 6(c). The frequency of the narrow spectral maximum associated with A_2 is slightly downshifted relative to $f_{t3}^A = 776.03$ kHz. By increasing z it increases slightly, from 774.8 to 775.7 kHz over the range z = 276.05 mm to 4 m, which corresponds to about 0.16 % and 0.04 % downshift relative to f_{t3}^A.

As discussed for Fig. 4(a), the spectral maximum at TS3 is accompanied by a narrow spectral notch at slightly higher frequency. This "upper frequency" notch is shifted slightly downwards in frequency by increasing z, from about 777.8 kHz to about 776.2 kHz over the range z = 276.05 mm to 4 m. As z increases, another spectral notch emerges at slightly lower frequency than the maximum, at about 774–774.5 kHz. This "lower frequency" notch is particularly prominent over the ranges z ≈ 0.75–1.25 m and z ≈ 2–3 m. As a result, close to the plate a spectral

"doublet" (maximum-minimum) occurs; developing into a spectral "triplet" (minimum–maximum-minimum) in the range 0.75–3 m.

Thus, in the TS3 frequency region the complex near-field extends to axial ranges of 4 m or more. From $|T(\eta, d, f)|$ given in Fig. 3 no event is identified that can be related to the "lower frequency" notch. This fact, together with the observation that the notch occurs only at relatively large distances from the plate, suggests that it is not due to wave interaction internally in the plate, but to destructive interference caused by the wave propagation in water.

In Fig. 6(d), in the TE2 frequency region, the frequency f_2 of the spectral maximum associated with A_3 is slightly upshifted relative to $f_{l2}^A = 955.37$ kHz. Over the range z = 276.05 mm to 4 m f_2 decreases slightly by increasing z, from 956.6 to 955.4 kHz. The upshift of f_2 as compared with f_{l2}^A is about 0.13 % and 0.05 %, for z = 276.05 and 376.05 mm, respectively. At 4 m f_2 is within the 100 Hz resolution as compared with f_{l2}^A. A similar slight monotonic downshift with increasing z is thus observed as reported by [3] for beam reflection. About ten times larger change with distance was however reported in [3]. Potentials in applications are discussed in Section 5.6.

In general, the measured spectral maxima and minima indicated by filled dots and open circle markers in Fig. 6 are in fair quantitative agreement with the simulations. Exceptions are the frequencies of the spectral maximum at the TS3 resonance, close to f_{t3}^A, cf. Fig. 6(c). For increasing z, two of the three measured frequencies are subject to small deviation from the simulated maximum "ridge", towards lower frequencies. The underlying causes of these deviations remain to be investigated.

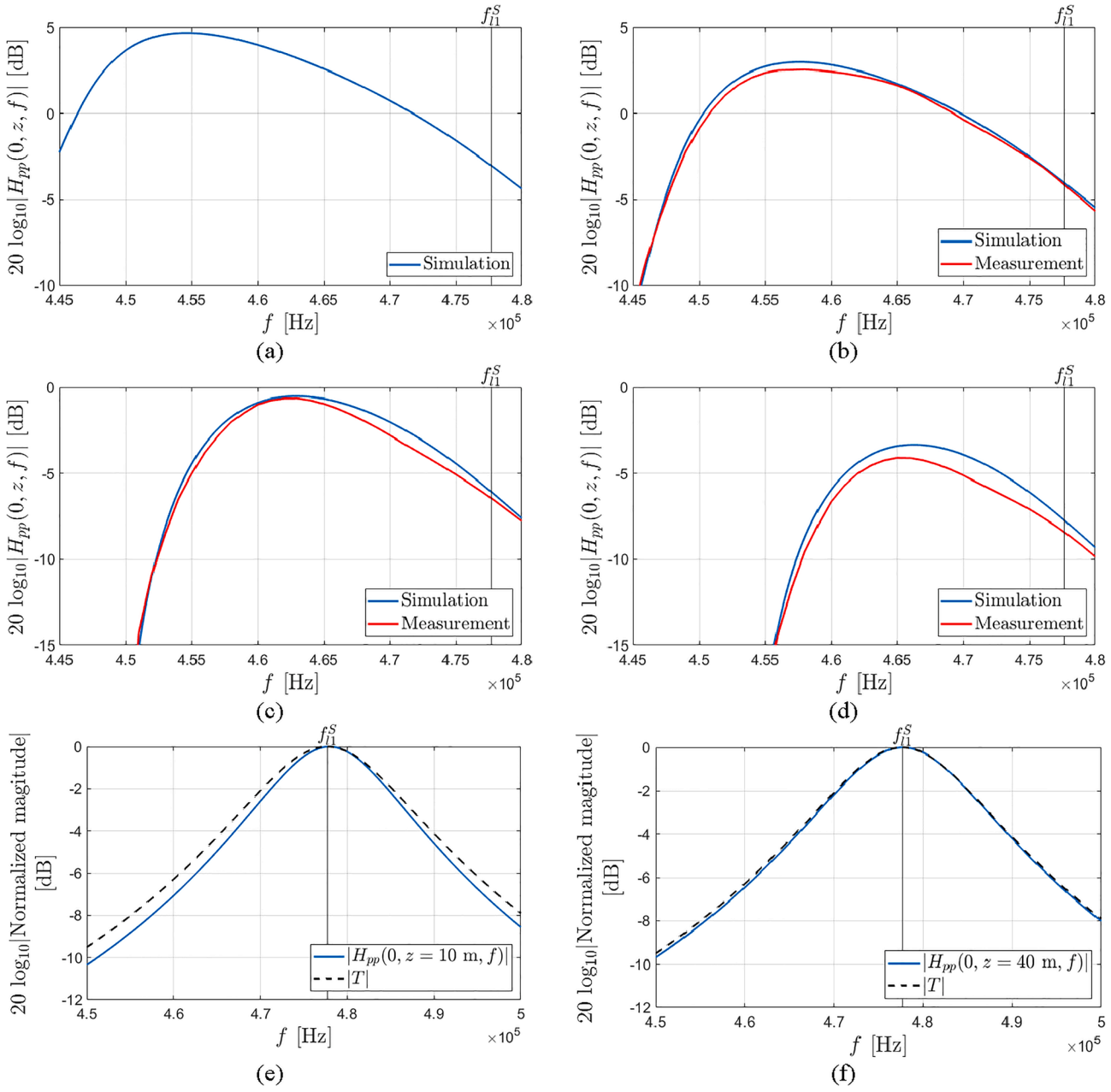

Fig. 7. Magnitude of the pressure transfer function $|H_{pp}(0,z,f)|$ shown in the TE1 frequency band, for increasing axial depth, z. (a) Simulated $|H_{pp}|$ at lower plate surface, z = 276.05 mm. Simulated and measured $|H_{pp}|$ at (b) z = 376.05 mm, (c) z = 626 mm, and (d) z = 875 mm. Simulated plane wave transmission coefficient, $|T(\eta = 0, d, f)|$, and normalized $|H_{pp}(0,z,f)|$ at (e) z = 10 m and (f) z = 40 m. f_{l1}^S is indicated with a vertical line in each plot.

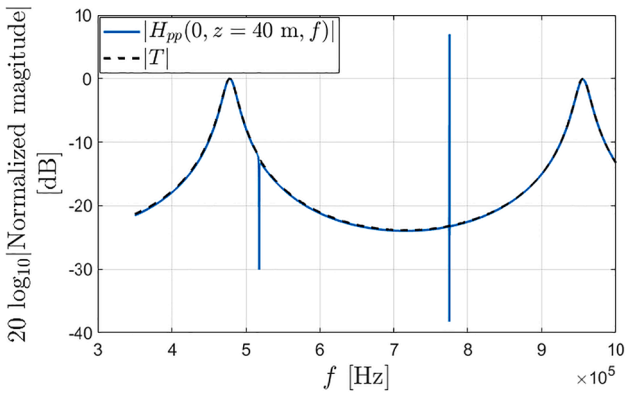

Fig. 8. Comparison of simulated and normalized pressure transfer function, $|H_{pp}(0,z,f)|$, for a beam normally incident to the plate, at $z = 40$ m; and the plane wave pressure transmission coefficient for a plane wave normally incident to the plate, $|T(\eta = 0,d,f)|$.

5.3. Near-field effects in $|H_{pp}|$ as compared to $|T|$

Fig. 7 (a)-(d) show the simulated $|H_{pp}(0,z,f)|$ for z = 276.05, 376.05, 626, and 875 mm, over the TE1 frequency band. Measurements are given at the three latter ranges. In parts (e) and (f), $|H_{pp}(0,z,f)|$ normalized to its maximum value is shown together with $|T(\eta = 0,d,f)|$, for z = 10 and 40 m, respectively. f_{l1}^S is indicated in each plot using a vertical line. Note that $H_{pp}(0,z,f)$ represents the axial response of the plate and subsequent fluid in the frequency - space domain for a sound beam propagating normally to the plate, whereas $T(\eta = 0,d,f)$ represents the response of the plate in the frequency - wavenumber domain for a plane wave propagating normally to the plate.

The $|H_{pp}|$ response is observed to be highly asymmetric from the plate to distances well in excess of z = 875 mm. This is ascribed to the notch appearing below f_1, discussed above. The measurements shown in parts (b)-(d) support the simulations. At these ranges $|H_{pp}|$ and $|T|$ are significantly different, and still differ at z = 10 m. By further increasing z, $|H_{pp}|$ attains a more symmetric response, which becomes almost identical to $|T|$ at $z = 40$ m, cf. Fig. 7(f). The results indicate that in the TE1 frequency band the normalized $|H_{pp}| \to |T|$ as $z \to \infty$, analogous to the asymptotic result reported by [4] for the reflected field, cf. Section 1. Very large z are however required before this occurs, due to significant near-field effects being influent to large ranges.

In Fig. 8, the simulated and normalized $|H_{pp}(0,z,f)|$ from Fig. 7(f) is plotted together with $|T(\eta = 0,d,f)|$ over the wider frequency range 350–1000 kHz. A rather close agreement is found, except for the very narrow spectral minimum and the maximum-minimum doublet in $|H_{pp}|$ close to TS2 and TS3, at about 517 kHz and 775 kHz. As discussed above, these are associated with the cutoff frequencies f_{t2}^S and f_{t3}^A, respectively, for the S_2 and A_2 Lamb modes. Corresponding minima and maxima are not present in $|T|$, since a plane wave at normal incidence cannot excite shear waves in the plate. The deviations between $|H_{pp}|$ and $|T|$ at 40 m shows that the near-field in radiation from the plate extends to very large ranges, especially in the frequency bands of the TS2 and TS3 plate resonances.

5.4. Non-monotonic f_1 shift in near- to far-field transition

Fig. 9 shows f_1 as a function of axial distance, z, extracted from three different spectra: $|p(0,z,f)|$, $|p(0,z,f)/f|$, and $|H_{pp}(0,z,f)|$. f_{l1}^S is indicated by the purple line denoted "T". The three curves approach constant values for large z. In Fig. 9(a), with ordinate range 30 kHz, the three curves are not distinguishable at long ranges. To emphasize the small but nonzero changes in f_1 at longer axial ranges, results for f_1 are shown in Fig. 9(b) to 500 m, at a smaller ordinate range of 600 Hz. The frequency resolution in extraction of f_1 is 1 Hz, obtained from the 20 Hz simulation resolution by 4th order polynomial interpolation and the least squares method.

In Fig. 9(b), the blue f_1 curve determined from $|p(0,z,f)|$ is found to be systematically higher than f_{l1}^S at long ranges. This is explained as follows. In the far-field of the plate, $|p(0,z,f)|$ may be expected to depend linearly on f, in a similar way as the piston far-field in a fluid without plate [52]. This hypothesis is confirmed by the black f_1 curve determined from $|p(0,z,f)/f|$, which approaches f_{l1}^S at large ranges. Consequently, the red f_1 curve determined from $|H_{pp}(0,z,f)|$ also approaches f_{l1}^S at large ranges, since z_0 at which $|p_i(0,z_0,f)|$ of Eq. (1) is evaluated is in the piston's far-field (at about 2.5 Rayleigh distances in the TE1 frequency range). However, since z_0 must be very large for $p_i(0,z_0,f)$ to exhibit a linear frequency dependency, a small deviation may be expected between f_1 extracted from $|p(0,z,f)/f|$ and $|H_{pp}(0,z,f)|$.

At the lower surface of the plate (z = 276.05 mm) f_1 is downshifted about 23 kHz (4.8 %) relative to f_{l1}^S, for all the three curves shown in Fig. 9(a). By increasing distance from the plate, the downshift of f_1 decreases up to z ≈ 6 m, at which f_1 is about equal to f_{l1}^S. For z in the range 6–500 m, f_1 overshoots f_{l1}^S. f_1 continues to increase up to z ≈ 11 m, and then decreases at larger distances. At z ≈ 11 m the overshoot of f_1 relative to f_{l1}^S is at its maximum, and approximately equal to 402, 250 and 252 Hz, respectively, for the curves labeled $p(0,z,f)$, $p(0,z,f)/f$, and $H_{pp}(0,z,f)$ in Fig. 9(b). At z = 500 m, f_1 extracted from $|p(0,z,f)|$, $|p(0,z,f)/f|$, and $|H_{pp}(0,z,f)|$ are about 202, 4, and 7 Hz higher than f_{l1}^S,

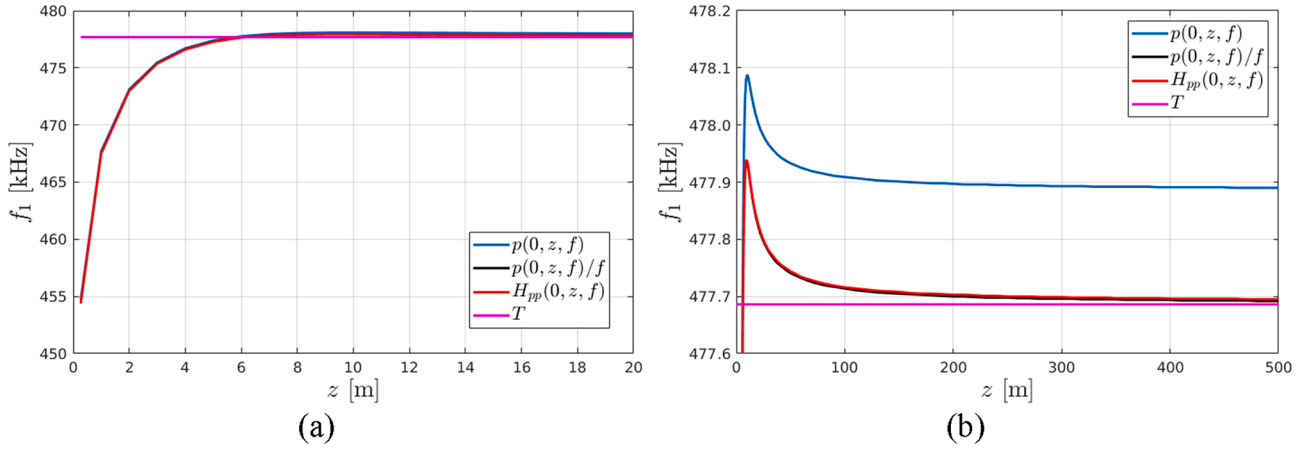

Fig. 9. The frequency of the spectral maximum in the TE1 frequency range, f_1, as determined from the simulated frequency spectra $|p(0,z,f)|$, $|p(0,z,f)/f|$, and $|H_{pp}(0,z,f)|$, shown as a function of axial distance, for z in the ranges (a) 276.05 mm to 20 m, and (b) 276.05 mm to 500 m. f_{l1}^S is indicated by the line denoted "T".

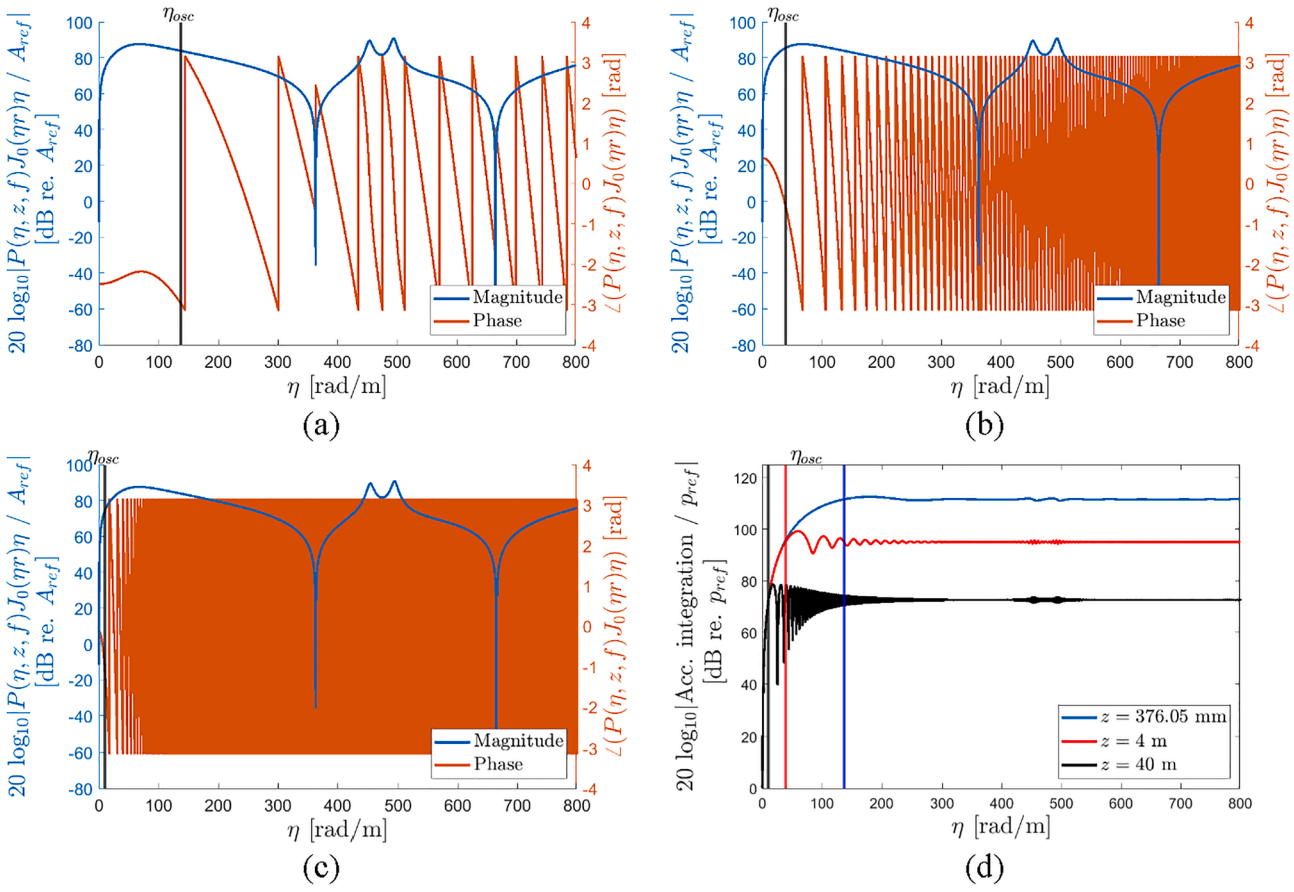

Fig. 10. Calculated magnitude and phase of the integrand $P(\eta,z,f)J_0(\eta r)\eta$ of Eq. (16), shown as a function of η for $f = 478$ kHz, at (a) z = 376.05 mm, (b) 4 m, and (c) 40 m. (d) Accumulated integrated pressure spectrum using Eq. (16), shown as a function of η for the same three values of z. The three η_{osc} values are marked with vertical lines in the figure, each one with color matching its corresponding curve.

respectively.

For beam transmission the f_1 approach to f_{11}^S is thus not monotonic as reported by [3,4] for beam reflection. Possible explanations for such deviation, and consequences in applications, are discussed in Section 5.6.

5.5. Far-field analysis of $|H_{pp}|$ as compared to $|\boldsymbol{T}|$

The results of Section 5.3 (Fig. 8) suggest that as $z\to\infty$, the normalized pressure transfer function $|H_{pp}(0,z,f)|$ may possibly approach the plane-wave transmission coefficient $|T(\eta = 0,d,f|$ over a wide frequency band 350–1000 kHz covering the TE1, TS2, TS3 and TE2 plate resonances, analogous to the asymptotic result reported by [4] for the reflected field in the TE1 region. It may be of some interest to examine this situation in some more detail. An analysis is here made for $f = 478$ kHz, close to f_{11}^S in the TE1 region. Similar analyses may be done for other frequencies in the band.

Fig. 10(a)-(c) show the magnitude and phase of the integrand of Eq. (16) normalized to the reference quantity A_{ref} = 1Pa·m/Hz, over the wavenumber range $\eta = 0-800$ rad/m, for z = 376.05 mm, 4 m, and 40 m. To investigate how the different wavenumber components contribute to the total integrated pressure spectrum, the accumulated integrated pressure spectrum component at 478 kHz is shown in Fig. 10(d), calculated at the mentioned 3 ranges using Eq. (16).

The red curve in Fig. 10(d) gives the 478 kHz accumulated integrated pressure spectrum component at z = 4 m normalized to the reference quantity p_{ref} = 1Pa/Hz, "oscillating" around the total integrated value of 95.0310 dB re. p_{ref}. Corresponding oscillations are observed also for the blue (z = 376.05 mm) and black (z = 40 m) curves. The oscillations are present throughout the η wavenumber range, but decrease in magnitude for larger η, at which the pressure spectrum converges towards the integrated pressure values 111.5327, 95.0310, and 72.6077 dB re. p_{ref}, for z = 376.05 mm, 4 m, and 40 m, respectively.

Because of the oscillatory nature of the integrand, these pressure values are also found at specific low wavenumber values, η_{osc}, indicated in Fig. 10(a)-(d) by the vertical lines. The η_{osc} values given are 136.5854, 38.6406, and 10.4118 rad/m, for z = 376.05 mm, 4 m, and 40 m, respectively. Wavenumber components larger than η_{osc} will ultimately cancel during the integration using Eq. (16), due to the oscillatory nature of the integrand. That means, the integral over the wavenumber range (η_{osc},∞) is zero. The non-zero plane wave contributions to the integrated pressure spectrum thus come from the region $\eta < \eta_{osc}$. (This argumentation is similar to the one used in the stationary phase method for oscillating integrals, cf. e.g. [53].).

From Fig. 10(d), it is observed that the η region $(0,\eta_{osc})$ contributing to the integrated pressure spectrum decreases by increasing z. That is, η_{osc} is largest for z = 376.05 mm, and smallest for z = 40 m. From this it may be hypothesized that beam simulations at large z become more similar to a plane wave propagating normally to the plate (for which $\eta = 0$) than simulations at small z. This hypothesis is largely confirmed by the simulation results of Fig. 7(f) in the TE1 frequency range, and by Fig. 8 over most of the frequency range 350–1000 kHz. The exceptions are the two highly narrow frequency bands at the TS2 and TS3 plate resonances in Fig. 8. These are subject to discussion in Section 5.6.

5.6. Discussion

The main findings for a beam interacting with the plate at normal

beam incidence can be summarized as follows:

For the leaky Lamb mode associated with the TE1 plate resonance at f_{l1}^S, the frequency of its maximum, f_1, is downshifted about 4.8 % at the plate, relative to f_{l1}^S. By increasing distance from the plate, f_1 approaches f_{l1}^S from below. At larger ranges f_1 becomes slightly higher than f_{l1}^S (up to about 0.5 ‰) and then approaches f_{l1}^S from above as $z \to \infty$. Very large distances are required before $f_1 \approx f_{l1}^S$. For beam transmission the f_1 approach to f_{l1}^S is thus not monotonic as reported by [3,4] for beam reflection. Possible explanations for such deviation may be the limited plate-receiver range investigated by [3,4], possible different $h_f a$ number, or that by these authors the source-plate and plate-receiver distances were varied simultaneously. The results are essential for finite-aperture correction when TE1 is used for accurate immersion measurement of plate thickness and/or compressional-wave sound velocity, cf. Section 1.

In the frequency band of TE1, at slightly lower frequency than f_1, a narrow minimum ("notch") is revealed for z in the range of about 0.35–3.4 m, at a frequency which varies with range, z. It is evident that the notch is caused by leaky ultrasonic guided plate waves interacting with the finite angular spectrum of the beam. Clarification of the underlying physical causes of the notch in more detail requires further investigations. The fact that it does not exist at the plate surface suggests that it may be related to water-borne interference, as discussed above. The notch will significantly affect the transmitted beam over approximately a 20 kHz frequency band close to f_1 and TE1.

The simulations show that due to bounded beam interaction with the backward-wave branch in the frequency band of TE1, the near-field of the transmitted wavefield extends to very far axial distances. As $z \to \infty$, $|p|$ approaches a spherical divergence (1/z) axial distance dependency. Very large distances z are however required before this far-field characteristic is reached: at z = 40 and 500 m the deviations from spherical divergence (1/z) are found to be about 0.5 and 0.01 dB, respectively.

For the leaky Lamb mode associated with the TS2 plate resonance at f_{t2}^S, the frequency of the narrow and significant minimum ("notch") in $|H_{pp}|$ observed close to the plate [18,27,28], is found to be practically constant for all z investigated. The notch is caused by the beam's finite angular spectrum, where the beam's plane wave components at oblique angle of incidence excite shear waves in the plate. Use of finite-aperture ultrasonic transducers in combination with TS2 (i.e., f_{t2}^S) for accurate immersion measurement of thickness or shear-wave velocity of the plate, thus appears promising for a range of measurement distances, from the close near-field to the far-field of the plate, without need for finite-aperture correction nor other efforts to achieve plane-wave conditions.

In the frequency band of the leaky Lamb mode associated with the TS3 plate resonance at f_{t3}^A, a relatively complex near-field is revealed for $|H_{pp}|$ extending to z = 4 m or more. A spectral maximum due to shear waves in the plate dominates close to the plate, with frequency close to f_{t3}^A. By increasing z into the near-field, a narrow spectral "doublet" (maximum-minimum) evolves, further developing into a narrow spectral "triplet" (minimum-maximum-minimum) at larger z. Use of finite-aperture transducer with the spectral maximum may have potentials for immersion measurement of thickness or shear wave velocity of the plate. Use of finite-aperture transducers may require finite-aperture correction when very high accuracy is required.

For the leaky Lamb mode associated with the TE2 plate resonance at f_{l2}^A, a slight upshift of f_2 is found relative to f_{l2}^A. The difference $f_2 - f_{l2}^A$ decreases by increasing distance, from about 1.3 ‰ at the plate to less than 0.1 ‰ at z = 4 m. This is a similar trend as reported by [3] for beam reflection, but ten times larger change with distance was reported in [3]. That could possibly be due to different $h_f a$ number. For the relatively high $h_f a$ number used here (about 42.6 at f_{l2}^A), accurate immersion measurement of thickness or compressional-wave velocity of the plate thus appears promising at a range of distances from the plate into the far-field, using finite-aperture ultrasonic transducers in combination with TE2 (i.e., f_{l2}^A). No finite-aperture correction nor other efforts to achieve plane-wave conditions appears to be needed, except for measurement close to the plate when very high accuracy is required. To which extent such a conclusion will be affected by using a source transducer with lower $h_f a$ number, remains to be investigated.

In the near-field, $|H_{pp}|$ deviates significantly from $|T|$, for all leaky Lamb modes involved. As $z \to \infty$, the normalized $|H_{pp}|$ is shown to closely approach the $|T|$ response over the 350–1000 kHz frequency band addressed. These asymptotic features are explained in terms of the ASM model, cf. Section 5.5. At z = 40 m some deviations are still observed, however, related to the TS2 and TS3 modes.

An interesting question in this context (of more principal than practical importance, perhaps) is whether the normalized $|H_{pp}|$ will actually approach $|T|$ at all frequencies in the band 350–1000 kHz as $z \to \infty$. That is, whether the narrow spectral minimum and maximum-minimum doublet associated with TS2 and TS3 observed in Fig. 8, respectively, will actually vanish in $|H_{pp}(0,z,f)|$ as $z \to \infty$. According to the analysis of Section 5.5, a non-zero η will generate shear waves in the plate, and in that case the normalized $|H_{pp}(0,z,f)| \neq |T(\eta = 0, d, f|$ at these frequencies. For the shear waves to vanish, η has to be zero, for which the integral of Eq. (16) is zero, and thus $|H_{pp}(0,z,f)| = 0$. A more thorough analysis of this case remains.

The phenomena discussed above for frequency regions of different Lamb modes will depend on a range of parameters. Examples are the source-plate distance (determining near- to far-field transition effects in the field of the source transducer), the plate-receiver distance (determining near- to far-field transition effects in the plate's transmitted field, as discussed here), the $h_f a$ number of the source transducer field (and thus the angular spectrum of the incident field) [26], the plate's Poission number [28], intrinsic losses in the plate and water [28], the aperture of the receiving transducer [30], and the angle of beam incidence [21–23].

6. Conclusions

Prior literature on bounded-beam transmission through a water-embedded steel plate has revealed anomalous phenomena in the transmitted sound pressure field close to the plate. The phenomena are caused by diffraction due to the finite angular spectrum of the incident beam, interacting with leaky Lamb waves being excited (by the beam) to propagate in the plate. The present analysis extends earlier work by investigating these complex bounded-beam phenomena in an analysis of the near- to far-field transition of the plate's transmitted field, for normal beam incidence to the plate. The field quantity studied is the axial pressure transfer function through the plate, $|H_{pp}(0, z, f)|$. The analysis is conducted over the 350–1000 kHz frequency band of leaky Lamb modes corresponding to the S_2, A_2, and A_3 Lamb modes of a 6.05 mm thick plate.

An angular spectrum method (ASM) is presented and used to describe propagation of the sound field radiated by a circular, baffled, and uniformly vibrating piston source, through a fluid-embedded isotropic elastic solid plate of infinite extent, at normal beam incidence to the plate. For the piston with 10.55 mm radius used here, the $h_f a$ number, −3dB angle, and source-plate distance are in the ranges 15.6–44.6, 5.9−2.1°, and 3.3–1.2 Rayleigh distances, respectively, over the frequency band considered. For this case, the simulations show that for certain leaky Lamb modes, the near-field of the transmitted wavefield extends to very far axial distances. This is so especially in the frequency bands of TE1 and TS3.

Close to TE1, the downshift of the resonance frequency f_1 relative to f_{l1}^S is significant to about 6 m. At longer ranges a slight upshift is experienced, before $f_1 \to f_{l1}^S$ as $z \to \infty$. Nearfield influences are observed to hundreds of meters. A significant and influent notch below and close to f_1 is observed in the range z = 0.35–3.4 m. In the frequency band of TS3, a complex nearfield extends to at least z = 4 m, including a spectral

maximum-minimum doublet close to the plate, and a minimum–maximum-minimum triplet at longer ranges. In the frequency band of TE2, a slight up-shift of the resonance frequency f_2 relative to f_{l2}^A is observed in the close vicinity of the plate, which decreases rapidly by increasing range, z. For the TS2 plate resonance, no frequency shift of the resonance frequency is observed. In the near-field, the normalized $|H_{pp}(0,z,f)|$ deviates significantly from the plane-wave pressure transmission coefficient $|T(\eta,d,f)|$, for all leaky Lamb modes considered. For very large axial ranges the normalized $|H_{pp}|$ approaches $|T|$. At z = 40 m there are still some deviations, however, in the narrow frequency bands of TS2 and TS3.

In general, the simulation results are supported by measurement results at three axial distances, about 10, 35, and 60 cm from the plate (z = 376.05, 626 and 875 mm, respectively). Some deviations are experienced in modelling of details for precise description of the two frequency bands close to the TS2 and TS3 plate resonances.

The results are of importance for experimental characterization of plates and materials using e.g. the through-transmission resonance method, cf. Sections 1 and 5.6. The ASM model presented here provides potentials for calculation of finite-aperture corrections in measurement situations for which such are required, including the effects of a finite-aperture receiving transducer [30].

Declaration of Competing Interest

The authors declare that they have no known competing financial interests or personal relationships that could have appeared to influence the work reported in this paper.

Acknowledgement

The authors wish to acknowledge Magne Vestrheim, University of Bergen, for stimulating discussions and valuable input during the work described.

References

[1] T.J. Plona, L.E. Pitts, W.G. Mayer, Ultrasonic bounded beam reflection and transmission effects at a liquid/solid - plate/liquid interface, J. Acoust. Soc. Am. 59 (6) (1976) 1324–1328, https://doi.org/10.1121/1.381011.
[2] K.W. Ng, T.D.K. Ngoc, J.A. McClure, W.G. Mayer, Nonspecular transmission effects for ultrasonic beams incident on a solid plate in a liquid, Acta Acust. United Acust. 48 (3) (1981) 168–173.
[3] R. K. Johnson, A. J. Devaney, Transducer model for plate thickness measurement, in: Proc. IEEE Intern. Ultras. Symp., San Diego, CA, USA, 27-29 Oct. 1982, pp. 502–504.
[4] N. A. Whitaker, Jr. and H. A. Haus, Backward wave effects in acoustic scattering measurements, in: Proc. IEEE Ultras. Symp., Atlanta, GA, USA, 31 Oct. - 2 Nov. 1983, pp. 891-894.
[5] J.M. Claeys, O. Leroy, Reflection and transmission of bounded sound beams on half-spaces and through plates, J. Acoust. Soc. Am. 72 (2) (1982) 585–590, https://doi.org/10.1121/1.388039.
[6] M. Deschamps, P. Chevee, Reflection and transmission of a transient bounded beam by a dispersive and orthotropic plate, Acta Acust. 1 (122) (1993) 3–14.
[7] K. Van Den Abeele, O. Leroy, On the influence of frequency and width of an ultrasonic bounded beam in the investigation of materials: Study in terms of heterogeneous plane waves, J. Acoust. Soc. Am. 93 (5) (1993) 2688–2699.
[8] D.E. Chimenti, J.-G. Zhang, S. Zeroug, L.B. Felsen, Interaction of acoustic beams with fluid-loaded elastic structures, J. Acoust. Soc. Am. 95 (1) (1994) 45–59, https://doi.org/10.1121/1.408340.
[9] S. Zeroug, L.B. Felsen, Nonspecular reflection of two- and three-dimensional acoustic beams from fluid-immersed plane-layered elastic structures, J. Acoust. Soc. Am. 95 (6) (1994) 3075–3089, https://doi.org/10.1121/1.409999.
[10] M.J. Anderson, P.R. Martin, C.M. Fortunko, Resonant transmission of a three-dimensional acoustic sound beam through a solid plate in air: Theory and measurement, J. Acoust. Soc. Am. 98 (5) (1995) 2628–2638, https://doi.org/10.1121/1.413229.
[11] O.I. Lobkis, A. Safaeinili, D.E. Chimenti, Effects of diffraction and experimental geometry on acoustic beam reflection from a fluid-loaded plate: a 3-D analysis, Ultrasonics 34 (2) (1996) 477–481, https://doi.org/10.1016/0041-624X(95)00126-N.
[12] P. Cawley, B. Hosten, The use of large ultrasonic transducers to improve transmission coefficient measurements on viscoelastic anisotropic plates, J. Acoust. Soc. Am. 101 (3) (1997) 1373–1379, https://doi.org/10.1121/1.418103.
[13] B.J. Landsberger, M.F. Hamilton, Second-harmonic generation in sound beams reflected from, and transmitted through, immersed elastic solids, J. Acoust. Soc. Am. 109 (2) (2001) 488–500, https://doi.org/10.1121/1.1318777.
[14] S.J. Younghouse, Irradiation of an elastic plate by a finite-amplitude sound beam with applications to nondestructive evaluation, PhD thesis, University of Texas, Austin, TX, USA, 2002.
[15] S.D. Holland, D.E. Chimenti, Air-coupled acoustic imaging with zero-group-velocity Lamb modes, Appl. Phys. Lett. 83 (13) (2003) 2704–2706, https://doi.org/10.1063/1.1613046.
[16] D. Fei, D.E. Chimenti, S.V. Teles, Material property estimation in thin plates using focused, synthetic-aperture acoustic beams, J. Acoust. Soc. Am. 113 (5) (2003) 2599–2610.
[17] J. Jocker, D. Smeulders, Minimization of finite beam effects in the determination of reflection and transmission coefficients of an elastic layer, Ultrasonics 46 (1) (2007) 42–50, https://doi.org/10.1016/j.ultras.2006.10.001.
[18] K. D. Lohne, P. Lunde, and M. Vestrheim, Ultrasonic signal transmission in plates - Study of a steel plate immersed in water, Proc. 31th Scand. Symp. Phys. Acoust., Geilo, Norway, 27-30 Jan., 2008, 23 p.
[19] K. D. Lohne, P. Lunde, and M. Vestrheim, Measurements and 3D simulations of ultrasonic directive beam transmission through a water-immersed steel plate, in: Proc. 34th Scand. Symp. Phys. Acoust., Geilo, Norway, 29 Jan.-2 Feb., 2011, 29 p.
[20] M. Aanes, K. D. Lohne, P. Lunde, M. Vestrheim, Normal incidence ultrasonic beam transmission through a water-immersed plate using a piezoelectric transducer. Finite element modeling, angular spectrum method and measurements, in: Proc. 19th Intern. Congr. Sound Vibr., Vilnius, Lithuania, 2012, pp. 12–20, July 8-12 2012.
[21] M. Aanes, K. D. Lohne, P. Lunde, M. Vestrheim, Ultrasonic beam transmission through a water-immersed plate at oblique incidence using a piezoelectric source transducer. Finite element - angular spectrum modeling and measurements, in: Proc. IEEE Intern. Ultras. Symp., Dresden, Germany, 7-10 Oct., 2012, pp. 1972–1977, https://doi.org/10.1109/ULTSYM.2012.0494.
[22] M. Aanes, P. Lunde, and M. Vestrheim, Ultrasonic beam transmission through a steel plate at oblique incidence. Uniform piston vs. piezoelectric transducer, in: Proc. 36th Scand. Symp. Phys. Acoust., Geilo, Norway, 3-6 Feb., 2013, 36 p.
[23] M. Aanes, Interaction of piezoelectric transducer excited ultrasonic pulsed beams with a fluid-embedded viscoelastic plate. Finite element modeling, angular spectrum modeling and measurements, PhD thesis, University of Bergen, Bergen, Norway, 2014.
[24] M. Aanes, K. D. Lohne, P. Lunde, M. Vestrheim, Transducer beam diffraction effects in sound transmission near leaky Lamb modes in elastic plates at normal incidence, in: Proc. IEEE Intern. Ultras. Symp., Taipei, Taiwan, 21-24 Oct., 2015, 4 p., https://doi.org/10.1109/ULTSYM.2015.0021.
[25] G. Waag, L. Hoff, P. Norli, Air-coupled ultrasonic through-transmission thickness measurements of steel plates, Ultrasonics 56 (2015) 332–339, https://doi.org/10.1016/j.ultras.2014.08.021.
[26] M. Aanes, K. D. Lohne, P. Lunde, M. Vestrheim, Finite aperture influence on energy concentration, frequency shift, and signal enhancement, for acoustic transmission in the negative group velocity region of the S1 leaky Lamb mode, in: Proc. IEEE Intern. Ultras. Symp., Tours, France, 11-16 Sep., 2016, 4 p., https://doi.org/10.1109/ULTSYM.2016.7728741.
[27] M. Aanes, K. D. Lohne, P. Lunde, and M. Vestrheim, Beam diffraction effects in sound transmission of a fluid-embedded viscoelastic plate at normal incidence, J. Acoust. Soc. Am. **140** (1) (2016) EL67–EL72, https://doi.org/10.1121/1.4954893.
[28] M. Aanes, K.D. Lohne, P. Lunde, M. Vestrheim, Beam diffraction effects in the backward wave regions of viscoelastic leaky Lamb modes for plate transmission at normal incidence, IEEE Trans. Ultrason. Ferroelectr. Freq. Control 64 (10) (2017) 1558–1572, https://doi.org/10.1109/TUFFC.2017.2719627.
[29] E. V. Glushkov, N. V. Glushkova, and O. A. Miakisheva, Resonance transmission and backward leaky waves in the coupled system: Ultrasound transducer acoustic fluid immersed plate, Proc. Days on Diffraction, St. Petersburg, Russia, 19-23 June, 2017, pp. 134–140, https://doi.org/10.1109/DD.2017.8168011.
[30] S. H. Midtbø, Beam diffraction effects in guided-wave transmission of fluid embedded elastic plate. Influence of receiver distance and finite aperture, Master thesis, University of Bergen, Bergen, Norway, 2018, https://hdl.handle.net/1956/18465.
[31] E.V. Glushkov, N.V. Glushkova, O.A. Miakisheva, The distribution of air-coupled transducer energy among the traveling waves excited in a submerged elastic waveguide, Acoust. Phys. 65 (6) (2019) 623–633, https://doi.org/10.1134/S1063771019060034.
[32] E.V. Glushkov, N.V. Glushkova, O.A. Miakisheva, Backward waves and energy fluxes excited in acoustic medium with an immersed plate, Ultrasonics 94 (2019) 158–168, https://doi.org/10.1016/j.ultras.2018.10.001.
[33] T.J. Graham, J.D. Smith, A.P. Hibbins, J.R. Sambles, T.A. Starkey, Experimental characterization of acoustic beaming from an elastic plate by coupled symmetric leaky Lamb modes, Phys. Rev. B 104 (2021), 045105.
[34] A.H. Meitzler, Backward-wave transmission of stress pulses in elastic cylinders and plates, J. Acoust. Soc. Am. 38 (1965) 835–842.
[35] J. Wolf, T.D.K. Ngoc, R. Kille, W.G. Mayer, Investigation of Lamb waves having a negative group velocity, J. Acoust. Soc. Am. 83 (1) (1988) 122–126.
[36] P.L. Marston, Negative group velocity Lamb waves on plates and applications to the scattering of sound by shells, J. Acoust. Soc. Am. 113 (2003) 2659–2662.
[37] I.A. Nedospasov, V.G. Mozhaev, I.E. Kuznetsova, Unusual energy properties of leaky backward Lamb waves in a submerged plate, Ultrasonics 77 (2017) 95–99.
[38] A.M. Lomonosov, C. Nid, Z. Shen, Z. Li, Generation of negative group velocity Lamb waves by a moving laser source, Ultrasonics 99 (105950) (2019) 1–4.

[39] C. Prada, D. Clorennec, D. Royer, Local vibration of an elastic plate and zero-group velocity Lamb modes, J. Acoust. Soc. Am. 124 (1) (2008) 203–212.
[40] N. Stull, E. Flynn, M. Mascarenas, On the theoretical limitations in estimating thickness of a plate-like structure from a full-field single-tone response Lamb wave measurement, Ultrasonics 108 (106230) (2020) 1–11.
[41] T.E.G. Álvarez-Arenas, Simultaneous determination of the ultrasound velocity and the thickness of solid plates from the analysis of thickness resonances using air-coupled ultrasound, Ultrasonics 50 (2010) 104–109.
[42] D.E. Chimenti, Review of air-coupled ultrasonic materials characterization, Ultrasonics 54 (2014) 1804–1816.
[43] M. Castaings, B. Hosten, Air-coupled measurement of plane wave, ultrasonic plate transmission for characterising anisotropic, viscoelastic materials, Ultrasonics 38 (2000) 781–786.
[44] Y. Bouzidi, R.S. Douglas, A large ultrasonic bounded acoustic pulse transducer for acoustic transmission goniometry: Modeling and calibration, J. Acoust. Soc. Am. 119 (1) (2006) 54–64.
[45] E. Blomme, D. Bulcaen, F. Declercq, Recent observations with air-coupled NDE in the frequency range of 650 kHz to 1.2 MHz, Ultrasonics 40 (2002) 153–157.
[46] E.G. Williams, Fourier Acoustics: Sound Radiation and Nearfield Acoustical Holography, Academic Press, UK, 1999.
[47] V. Giurgiutiu, M.F. Haider, Propagating, evanescent, and complex wavenumber guided waves in high-performance composites, Materials 12 (2) (2019) 269, https://doi.org/10.3390/ma12020269.
[48] R. D. Mindlin, Waves and vibrations in isotropic, elastic plates, in: Structural Mechanics edited by J. N. Goodier and N. J. Hoff, Pergamon, New York, 1960, pp. 199–232.
[49] C. Prada, D. Clorennec, T.W. Murray, D. Royer, Influence of the anisotropy on zero-group velocity Lamb modes, J. Acoust. Soc. Am. 126 (2) (2009) 620–625, https://doi.org/10.1121/1.3167277.
[50] X. Yan, F.-G. Yuan, Conversion of evanescent Lamb waves into propagating waves via a narrow aperture edge, J. Acoust. Soc. Am. 137 (6) (2015) 3523–3533, https://doi.org/10.1121/1.4921599.
[51] S.-E. Hebaz, F. Benmeddour, E. Moulin, J. Assaad, Semi-analytical discontinuous Galerkin finite element method for the calculation of dispersion properties of guided waves in plates, J. Acoust. Soc. Am. 143 (1) (2018) 460–469, https://doi.org/10.1121/1.5021588.
[52] L.E. Kinsler, A.R. Frey, A.B. Coppens, J.V. Sanders, Fundamentals of Acoustics, 4th ed., J. Wiley & Sons, New York, USA, 2000.
[53] J.D. Achenbach, Wave propagation in elastic solids, Elsevier Science Pub, Amsterdam, The Netherlands, 1975.